Noninvasive molecular imaging of small living subjects using Raman spectroscopy

S. Keren, C. Zavaleta, Z. Cheng, A. de la Zerda, O. Gheysens, and S. S. Gambhir*

Molecular Imaging Program at Stanford, Departments of Radiology and Bioengineering, Bio-X Program, Stanford University, 1201 Welch Road, Stanford, CA 94305-5484

Edited by Michael E. Phelps, University of California, Los Angeles School of Medicine, Los Angeles, CA, and approved February 5, 2008 (received for review November 7, 2007)

Molecular imaging of living subjects continues to rapidly evolve with bioluminescence and fluorescence strategies, in particular being frequently used for small-animal models. This article presents noninvasive deep-tissue molecular images in a living subject with the use of Raman spectroscopy. We describe a strategy for small-animal optical imaging based on Raman spectroscopy and Raman nanoparticles. Surface-enhanced Raman scattering nanoparticles and single-wall carbon nanotubes were used to demonstrate whole-body Raman imaging, nanoparticle pharmacokinetics, multiplexing, and *in vivo* tumor targeting, using an imaging system adapted for small-animal Raman imaging. The imaging modality reported here holds significant potential as a strategy for biomedical imaging of living subjects.

nanotubes | SERS nanoparticles

Molecular imaging of living subjects provides the ability to study cellular and molecular processes that have the potential to impact many facets of biomedical research and clinical patient management (1–4). Imaging of small-animal models is currently possible by using positron emission tomography (PET), single photon emission computed tomography, magnetic resonance imaging, computed tomography, optical bioluminescence and fluorescence, high frequency ultrasound, and several other emerging modalities. However, no single modality currently meets the needs of high sensitivity, high spatial and temporal resolution, high multiplexing capacity, low cost, and high-throughput.

Fluorescence imaging, in particular, has significant potential for *in vivo* studies but is limited by several factors (5, 6), including a limited number of fluorescent molecular imaging agents available in the near infra-red (NIR) window with large spectral overlap between them, which restricts the ability to interrogate multiple targets simultaneously (multiplexing). In addition, background autofluorescence emanating from superficial tissue layers restricts the sensitivity and the depth to which fluorescence imaging can be used. Moreover, rapid photobleaching of fluorescent molecules limits their useful lifetime and prevents studies of prolonged duration. Therefore, we have attempted to develop new strategies that may solve some of the limitations of fluorescence imaging in living subjects.

Raman spectroscopy can differentiate the spectral fingerprint of many molecules, resulting in very high multiplexing capabilities. Narrow spectral features are easily separated from the broadband autofluorescence, because Raman is a scattering phenomenon as opposed to absorption/emission in fluorescence, and Raman active molecules are more photostable compared with fluorophores, which are rapidly photobleached. Unfortunately, the precise mechanism for photobleaching is not well understood. However, it has been linked to a transition from the excited singlet state to the excited triplet state. Photobleaching is significantly reduced for single molecules adsorbed onto metal particles because of the rapid quenching of excited electrons by the metal surface, thus preventing excited-state reactions and hence photobleaching (7). However, the inherently weak magnitude of the Raman effect (≈1 photon is inelastically scattered for every 10^7 elastically scattered photons) limits the sensitivity and, as a result, the biomedical applications of Raman spectroscopy. The discovery of the surface enhanced Raman scattering (SERS) phenomenon offers an exciting opportunity to overcome this lack of sensitivity and introduce Raman spectroscopy into new fields (8). SERS is a plasmonic effect where molecules adsorbed onto nano-roughened noble metal surfaces experience a dramatic increase in the incident electromagnetic field, resulting in high Raman intensities comparable to fluorescence (6).

Single-walled carbon nanotubes (SWNTS) also show an intense Raman peak produced by the strong electron–phonon coupling that causes efficient excitation of tangential vibration in the nanotubes quasi one-dimensional structure upon light exposure (9). Recent demonstrations of tumor targeting, using radiolabeled SWNTS (10) combined with low toxicity effects and rapid renal excretion (11), suggest that carbon nanotubes may also become promising molecular imaging agents for living subjects. Here, we report for the first time, to our knowledge, noninvasive imaging of SERS active nanoparticles [namely, Nanoplex Biotags (Oxonica) were used in this study and henceforth are referred to as SERS-biotags or biotags] and SWNT nanoparticles in small living subjects by using Raman spectroscopy. Instrument adaptation to small-animal imaging, quantification of reproducibility and sensitivity, pharmacokinetics of nanoparticles, demonstration of multiplexing, *in vivo* tumor targeting after tail-vein injection, and whole-body deep-tissue imaging are all established in this work.

Results

Optimization of Raman Imaging Instrumentation. Optical microscopes designed for surface imaging through transparent media face significant losses of light when imaging through a diffusive tissue because of light scattering. We used a Raman imaging setup based on a Renishaw InVia Raman microscope equipped with an excitation laser at 785 nm, which is typically used for surface imaging. Several measures were taken to optimize this setup specifically for small-animal imaging. A high numerical aperture (NA) objective, commonly used on this microscope setup, was found to be less than ideal when imaging small animals for both illumination and light collection. A small spot size illumination obtained by a high NA objective limits the permissible laser power that can be used before tissue damage. Moreover, high NA objectives collect light efficiently only from a small

Author contributions: S.K. and C.Z. contributed equally to this work; S.K., C.Z., and S.S.G. designed research; S.K., C.Z., Z.C., A.d.l.Z., and O.G. performed research; C.Z. analyzed data; and S.K., C.L.Z., and S.S.G. wrote the paper.

The authors declare no conflict of interest.

This article is a PNAS Direct Submission.

Freely available online through the PNAS open access option.

*To whom correspondence should be addressed. E-mail: sgambhir@stanford.edu.

This article contains supporting information online at www.pnas.org/cgi/content/full/0710575105/DCSupplemental.

spot size; a highly diffusive propagation of light photons through tissue results in only a very small number of scattered photons emanating from the same small spot size. For these reasons, we found that a ×12 open field lens with a defocused beam, resulting in a spot size of 20 × 200 μm, worked well. The spectral resolution was adjusted to allow high sensitivity while being able to multiplex different SERS nanoparticles by opening the monochromator slit (100-μm width) to obtain a spectral resolution of 10 cm^{-1}. A computer controlled stage was also added to the microscope setup to allow automated mapping of large surfaces. Raman images were obtained by using a Raman point-mapping method. The computer-controlled *x–y* translation stage performed a raster scan of a region of interest over the mouse, the Raman spectrum was measured at every point, and software algorithms were used to calculate the SERS nanoparticle concentration and generate a two-dimensional mapping image of the SERS nanoparticle distribution. Finally, a heated bed and an anesthesia inhalation unit were attached to the microscope stage to allow a long, motionless scan time at a stabilized body temperature. A photograph of the imaging setup is shown in supporting information (SI) Fig. S1*a*.

Raman Nanoparticles. The ideal properties of a nanoparticle used for small-animal Raman spectroscopy would include small dimensions, simple conjugation methods, no toxicity effects, and intense and unique Raman spectra. Recently developed SERS active nanoparticles, called Nanoplex Biotags (Oxonica), composed of a gold core, Raman-active molecular layer (see *Methods*), and silica coating, schematically shown in Fig. S1*b*, hold significant potential for *in vivo* imaging applications (12). The glass coating of these SERS nanoparticles guarantees physical robustness, insensitivity to environmental conditions, and simple biofunctionalization of the well studied silica surface chemistry. The SERS-nanoparticles were designed to maximize the Raman signal, and the NIR excitation and emission profiles are ideal for minimizing light absorption by tissue. SERS nanoparticles used in this study had a mean diameter of 120 nm, as seen in the transmission electron microscopy image in Fig. S2.

SWNTS exhibit a strong Raman peak at 1,593 cm^{-1}, which allows high sensitivity detection (Fig. S3). Unlike the SERS nanoparticles, these SWNTs are inherently Raman active and do not use a metal surface enhancer to increase Raman detection. The high aspect ratio of the carbon structure of SWNTs is ideal for bioconjugation, and recent reports have successfully shown specific tumor targeting *in vivo* within various tumor models, using various functionalized SWNTs (10, 13, 14). SWNTs have a very small diameter of ≈3 nm and a length of 200 nm, as schematically shown in Fig. S1*c* and on the atomic force microscopy image in Fig. S2*b*. SERS and SWNT nanoparticles were both tested for stability in mouse serum and incubated at 37°C over a 5-day period with no degradation of Raman signal detected (data not shown).

Imaging System Characterization. We demonstrated the *in vitro* and *in vivo* reproducibility of the measured and processed Raman spectra. Five samples (5-μl volume), each with 6.6 fmol of SERS nanoparticles, were measured on a piece of parafilm, using the Raman imaging setup. The coefficient of variance (COV) of the calculated SERS nanoparticle concentration, using the quantitative analysis method described in *Methods*, showed a reproducibility of 1.9%. Reproducibility was also evaluated in a nude mouse with four separate s.c. injections of 16 fmol of SERS nanoparticle (10-μl volume) mixed with a gelatinous protein mixture known as matrigel, which resembles the complex extracellular environment found in many tissues (10-μl volume). The matrigel was used to keep the SERS nanoparticles from diffusing quickly out of the skin and showed no inherent Raman spectra as expected (Fig. S4). The SERS nanoparticle component concentration calculated for different injection sites showed a COV of 3.1%. Deep tissue reproducibility was also determined by injecting 260 fmol of SERS nanoparticles (200-μl volume) via the tail-vein into three nude mice. Nanoparticles of various types are naturally taken up by the reticuloendothelial system and thus can be found in the Kupffer cells of the liver (15). The liver of each mouse was imaged ≈30 min after tail-vein injection, and component analysis revealed a COV of 16.7% between the three mice. Naturally, the higher variability could be attributed to a number of factors, such as positioning, injection technique, and individual animal pharmacokinetics. Reproducibility in the liver of a single mouse imaged repeatedly (eight times) showed a COV of 2.8% (data not shown).

Sensitivity was evaluated by s.c. injecting three mice with decreasing concentrations of SERS nanoparticles in a volume of 20 μl. The data revealed a highly linear relationship between calculated and injected concentration of nanoparticles with an $R^2 = 0.99$. The smallest amount of SERS nanoparticles detected in a 20-μl s.c. injection was 8.125 pM. *Ex vivo* measurements showed high linearity with $R^2 = 0.997$ and a detection limit as low as 600 particles (Fig. S5).

The maximum depth of penetration for our Raman microscope was evaluated by using a tissue mimicking phantom, where a maximum depth of 2 mm was observed by using 6 nM SWNTs and 5.5 mm, using 1.3 nM SERS nanoparticles (for more details, see *SI Text*). However, deeper penetration could be achieved by increasing administered nanoparticle concentration or slightly increasing the laser power while still remaining below exposure limits.

The effect of changing the working distance between the lens and the subject was also evaluated *ex vivo*, by changing the stage height that contained a 5-μl sample of 6.6 fmol of SERS nanoparticles and *in vivo* with a mouse that had been injected via tail vein, with a 200-μl sample of 260 fmol of SERS nanoparticles. The component concentration was found to increase exponentially as the sample per mouse on the stage was moved closer to the lens of the microscope (data not shown). However, calculated concentration only weakly depends on variations in objective-subject distance when detected through the diffusive mouse tissue.

Demonstration of SERS Nanoparticle Multiplexing in Mice. Each type of the SERS nanoparticles (Nanoplex biotags) contains a different Raman-active material with its own unique spectral fingerprint allowing detection and quantification of multiple tags simultaneously within the same animal. Two types, SERS 421 and SERS 440, with different Raman signatures were s.c. injected into a mouse to demonstrate the multiplexing capabilities in living subjects. The first s.c. injection consisted of 5 μl (6.6 fmol) of S421 and 15 μl of matrigel (Fig. 1*a*). The second s.c. injection consisted of 5-μl (6.6 fmol) of SERS 440 and 15 μl of matrigel (Fig. 1*b*). The third s.c. injection consisted of an equal mix of SERS 421 (5 μl), SERS 440 (5 μl), and 10 μl of matrigel (Fig. 1*c*). Based on their different Raman spectra, the concentration of each SERS nanoparticle could be calculated by using the component analysis method described later (see *Methods*). Fig. 1 shows the concentration mapping of the injection sites. The area of the three s.c. injections was mapped with a step size of 500 μm and an integration time of 1 s. The map shows the three individual injection sites; each assigned a color by the Nanoplex software based on their corresponding spectra, with the concentration magnitude portrayed as pixel brightness. Note that the third injection site was calculated to have a yellow color that correlates with an equal mix of the SERS 421 (red) and SERS 440 (green) SERS nanoparticles. *Ex vivo* experiments verifying the system's multiplexing capability are shown in Fig. S6.

In addition, we have been able to successfully multiplex four types of SERS Raman nanoparticles of varying concentrations in a living mouse. The first four s.c. injections consisted of 5 μl (6.6

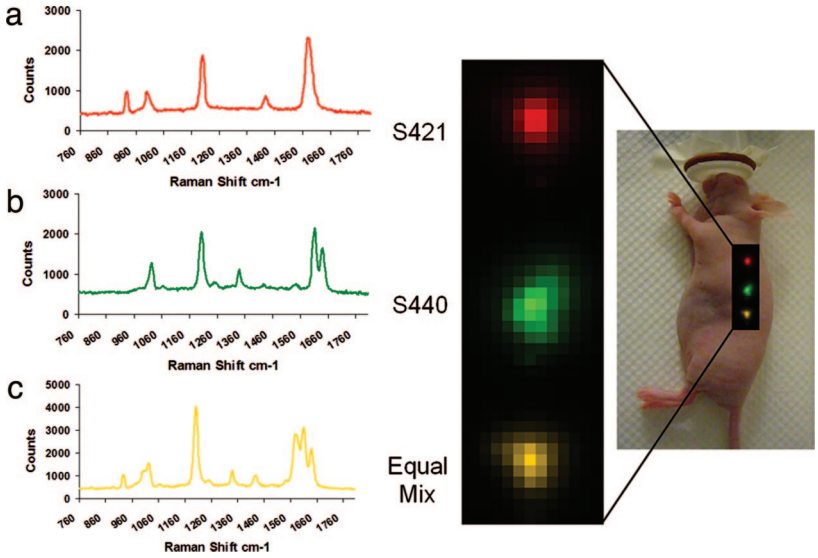

Fig. 1. Evaluation of multiplexing experiment. (*a*) Raman spectrum acquired from first s.c. injection of S421 SERS nanoparticles. The software has assigned the color red for this particular Raman spectrum. (*b*) Raman spectrum acquired from second s.c. injection of S440 SERS nanoparticles. The software has assigned the color green for this particular Raman spectrum. (*c*) Raman spectrum acquired from the third s.c. injection of an equal mix of S421 and S440. Notice how this spectrum represents an equal mix of both individual spectrums as if they had been overlaid. As a result, the color yellow is calculated by the analysis software to represent an equal mix of the red (S421) and green (S440) SERS nanoparticles in the map at *Right*.

fmol) of each SERS particle and 5 μl of matrigel as shown in Fig. S7*a* as follows: SERS 482 (green), SERS 420 (red), SERS 481 (yellow), and SERS 421 (blue). The fifth s.c. injection (purple) at the far right consisted of a mixture of these four SERS particles with varying concentrations to determine multiplexing *in vivo* (Fig. S7*a*). The mixture contained 4 μl of SERS 420 (5.28 fmol), 3 μl of SERS 421 (3.96 fmol), 2 μl of SERS 481 (2.64 fmol), 1 μl of SERS 482 (1.32 fmol), and 10 μl of matrigel. Based on their different Raman spectra, the concentration of each SERS nanoparticle could be calculated by using the component analysis method. Fig. S7 *b–e* show the four SERS components and the correlating intensity of the fifth injection site corresponding to the concentration of that particular component. The different intensities of the fifth injection site represented in each of the maps (Fig. S7 *b–e*) qualitatively correlates with the different concentrations of each SERS nanoparticle mixed. Notice how SERS 420 has the most intense pixel brightness in the fifth injection site (Fig. S7*c*), followed by SERS 421 (Fig. S7*e*) with the second most intense, then SERS 481 with the third most intense (Fig. S7*d*), and finally SERS 482 with the least intense at the fifth injection site (Fig. S7*b*). The area of the five s.c. injections was mapped with a step size of 750 μm and an integration time of 1 s. The map shows the five individual injection sites; each is assigned a color by the software based on their corresponding spectra, with the concentration magnitude portrayed as pixel brightness. The unique Raman spectra of these four different SERS nanoparticle are depicted in Fig. S8.

Liver Pharmacokinetics of SERS Nanoparticles and SWNTs. Taking advantage of the multiplexing capabilities of SERS nanoparticles detected by Raman spectroscopy, we studied the circulation properties of both pegylated and nonpegylated SERS nanoparticles simultaneously in living mice. An equal mixture of pegylated (PEG) and nonpegylated SERS nanoparticles (260 fmol of in a 200-μl volume), each with different Raman signatures, were tail-vein injected to evaluate their accumulation in the liver as a function of time. The laser was positioned over the mouse's liver before injection, and a Raman spectrum was acquired with a 10-s integration time over a period of 90 min. Quantitative analysis was used to calculate the relative concentration of the two different SERS nanoparticles, which nearly simultaneously accumulated in the liver (Fig. S9). The first group of mice ($n = 3$) that received an equal mix of 5 kDa of PEG and nonpegylated SERS nanoparticles showed no difference in liver accumulation between each of the nanoparticles and at 2 min after injection (Fig. 2*a*). The second group of mice ($n = 3$), which received an equal mix of 20 kDa PEG and nonpegylated SERS nanoparticles, also showed no difference in liver accumulation between each of the nanoparticles and plateaued at 4 min after injection (Fig. 2*b*). As with many nanoparticles administered intravenously, evading the macrophages of the reticuloendothelial system remains a constant problem, where in some *in vivo* cases pegylation is insufficient, as seen in our data and reported by Moghimi *et al.* The pharmacokinetics of SWNTs were also evaluated over a period of 90 min in 4 mice to reveal a fluctuation in nanotube distribution in the liver over the first 10 min followed by a continuous increase out to 90 min (Fig. 2*c*).

Whole-Body Noninvasive Imaging of SERS Nanoparticles. For whole-body mapping, mice were tail-vein injected with 260 fmol of SERS nanoparticles in a 200-μl volume. A raster scan was acquired 2 h after injection over a large portion of the mouse body with 1 mm step size and 3 s integration time. Quantitative analysis software calculated the concentration of SERS nanoparticles and generated an image showing accumulation of the SERS nanoparticles in the liver (Fig. 3*a*). A finer mapping with step size of 750 μm over the liver region reveals a detailed image of the liver. A slight distinction between liver lobes can be seen in this higher resolution image (Fig. 3*b*). SERS nanoparticles were visualized in the liver region out to 24 days after tail-vein injection, and continued to produce a recognizable spectrum with sustainable intensity for 24 days. Killed animals underwent *ex vivo* tissue analysis, and we confirmed the presence of SERS nanoparticles in the liver of mice (data not shown).

Whole-Body Noninvasive Imaging and Tumor Targeting of SWNTs. SWNTs were also imaged in nude mice after tail-vein injection of $\approx$60 pmol in 200 μl. An intense peak at 1593 cm^{-1} makes nanotubes easily detected with Raman spectroscopy. A Raman image was acquired with a raster scan 2 h after injection with a step size of 1

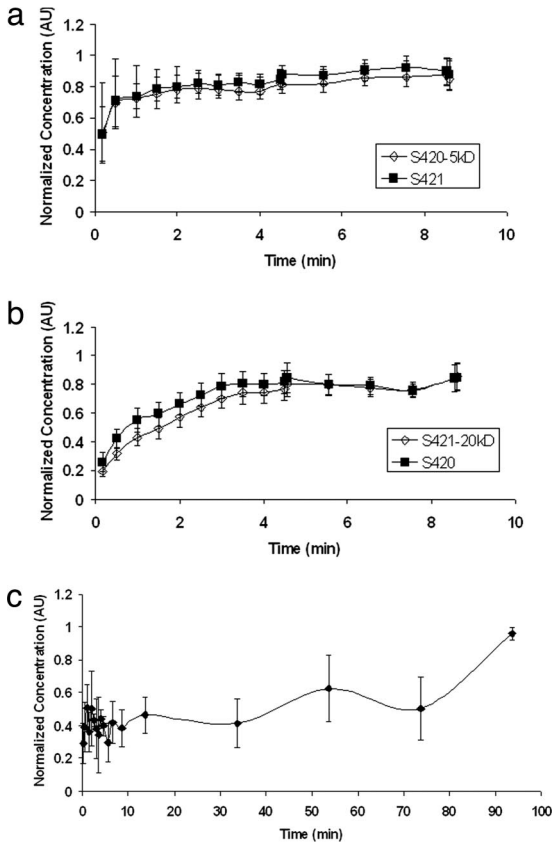

Fig. 2. Pharmacokinetics of SERS nanoparticles and SWNTs in the liver [data acquisition starts at 10 s, zero accumulation at time point zero (data not shown)]. (*a*) Accumulation of nonpegylated SERS versus 5 kDa of PEG SERS nanoparticles in liver of nude mouse. The graph depicts the mean normalized concentration of SERS nanoparticles in three mice ± SEM. (*b*) Accumulation of nonpegylated SERS versus 20 kDa of PEG SERS nanoparticle in liver of nude mouse. The graph depicts the mean normalized concentration of SERS nanoparticles in three mice ± SEM. (*c*) Pharmacokinetics of nanotubes in liver evaluated >90 min after tail-vein injection. The graph depicts the mean normalized concentration of nanotubes in four mice ± SEM. Note the gradual increase of SWNT accumulation in liver after 30 min after injection.

mm and an integration time of 3 s. The map revealed accumulation of nanotubes in the liver and a random distribution faintly dispersed across the peritoneal cavity (Fig. S10*a*). The SWNTs were also evaluated daily for liver accumulation and showed an increase in Raman intensity several days after tail-vein injection. Because of this continuous rise in Raman signal in the liver, another map of the same area, using the same image acquisition parameters, was taken at 72 h after injection to reveal a better defined liver with better delineation of the liver than the previous 2 h image of the same area (Fig. S10*b*). Daily evaluation of the liver continued to show Raman signal in the liver until 12 days after injection, at which time the animals were killed. Killed animals underwent *ex vivo* tissue analysis, and we confirmed the presence of nanotubes in the liver of mice (data not shown).

Furthermore, preliminary data demonstrated the ability of our modified Raman microscope to detect targeting of SWNTs conjugated with arginine-glycine-aspartate (RGD) peptide in an integrin positive U87MG tumor model in living mice. This RGD peptide binds to $\alpha_v\beta_3$ integrin, which is overexpressed in angiogenic vessels and various tumor cells (16). Tumor targeting of RGD SWNTs was described by Liu *et al.* (10), using microPET imaging and *ex vivo* Raman imaging of tissues. Six mice, s.c. inoculated with 2×10^6 U87MG cells near the right shoulder were divided into two groups. The first group (experimental) received a tail-vein injection

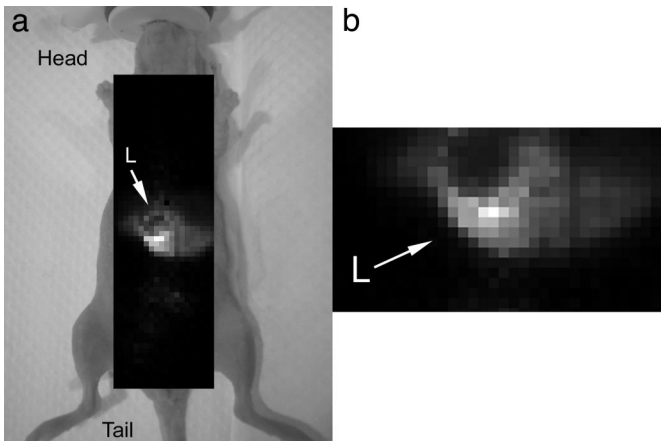

Fig. 3. Raster-scan image of mouse liver, using Raman spectroscopy in conjunction with SERS nanoparticles. (*a*) Whole-body map (1-mm steps) of nude mouse 2 h after tail-vein injection of SERS nanoparticles. Note how most of the SERS particles accumulated in the liver (L) (arrow), resulting in a well defined image. (*b*) Map of liver (750-μm steps), showing higher definition of liver (arrow) and slight distinction between the two liver lobes.

of RGD conjugated SWNTs of ≈60 pmol in 200 μl. The second group (control) received an i.v. injection of plain nontargeted SWNTs of the same concentration. Raster scans were acquired at 24 h after SWNT injection over the tumor area with 750-μm steps to generate Raman images (Fig. 4*a*). The images revealed an intense accumulation of RGD conjugated SWNTs in the tumor area; however, little to no accumulation of plain SWNTs was observed in the tumor area at 24 h after injection. Raman spectra were taken in living mice at 24 h after injection and revealed a significant increase ($P < 0.05$) in SWNT accumulation in the tumor areas of experimental mice receiving RGD SWNTs (SWNT concentration: 0.0204 ± 0.0087) compared with the control group receiving plain SWNTs (SWNT concentration: 0.0016 ± 0.0005) (Fig. 4*b*).

Discussion

In summary, we adapted a Raman microscope to demonstrate Raman imaging of small living subjects while using two different types of Raman nanoparticles, SERS active nanoparticles (Nano-

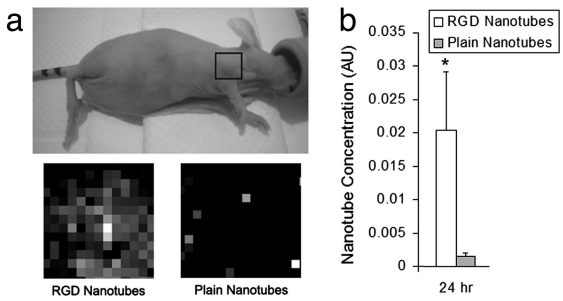

Fig. 4. Accumulation of RGD SWNTs and plain nontargeted SWNTs within an integrin-positive U87MG tumor model at 24 h after i.v. injection. (*a*) Digital photograph of mouse depicting tumor area (black square) and corresponding Raman images acquired 24 h after SWNT injection by raster scan with 750-μm steps. Notice the accumulation of RGD SWNTs in the tumor area as opposed to the plain nontargeted SWNTs that show little to no accumulation in the tumor area. (*b*) Raman spectral analysis of RGD nanotubes and plain nontargeted nanotubes within the tumor at 24 h after SWNT injection. The graphed data show a significant increase (*, $P < 0.05$) in Raman signal in mice ($n = 3$ per group) injected with RGD nanotubes as opposed to mice injected with plain nanotubes, thus indicating accumulation of RGD SWNT to tumor site. This quantitative data supports the Raman images displayed in *a*.

plex Biotags), and SWNTs. We have shown relatively high signal reproducibility both *in vitro* and in living subjects and the ability to produce an image of nanoparticles from both s.c. locations and from deeper tissues (e.g., liver) in living mice. Furthermore, we have demonstrated the ability to follow the arrival of nanoparticles in liver tissue to create time–activity curves. A minimum detection sensitivity of 8.125 pM was observed in a living mouse while using SERS nanoparticles. The ability to multiplex with four SERS nanoparticles presenting different Raman spectra was also demonstrated with the rapid and straightforward distinction between these nanoparticles in living mice. These initial results are encouraging and demonstrate the potential robustness of a Raman-based imaging strategy for small living subjects.

In the current proof-of-principle work, we demonstrated detection of Raman nanoparticles in both superficial and deep tissues along with an initial evaluation of its potential to detect tumor targeting with SWNTs conjugated to RGD peptide in an U87MG animal model. The primary limitation to Raman imaging of larger subjects will be those also faced by other optical techniques and is limited by NIR light penetration beyond a few centimeters of tissue (17). The key advantages of the current Raman imaging strategy over fluorescence is the very high multiplexing capability and lack of confounding background signal from autofluorescence. A study by Souza *et al.* (18) was able to collect a Raman spectra from the surface of a mouse (without forming any images) but had to use intratumoral injection of nanoparticles and also a very large concentration (3.8 μM) of Raman nanoparticles in a relatively large volume of 300 μl (18). Another group has applied multiple Raman signals to follow the distribution of cholesterol in a rat eye while showing the phenotyping of lymphocytes by using a single nonenhanced Raman-labeled (filipin) polystyrene bead to monitor cholesterol in a rat eye in conjunction with the inherent Raman peak associated with proteins to follow the distribution of cholesterol (19). Furthermore, it was shown that these Raman-labeled polystyrene spheres could be successfully used in combination with a fluorescent label. Using an additional Raman label, can overcome the many limitations that arise with fluorescence such as photobleaching, autofluorescence, and a limited number of fluorescent labels. Although we demonstrated multiplexing with only four SERS nanoparticles, we should be able to easily image many more simultaneously injected SERS nanoparticles, and as many as 10 spectrally distinct SERS nanoparticles are already available (e.g., Oxonica).

Glass-encapsulated SERS active nanoparticles are only one kind of Raman particle recently developed that can be used as contrast agents for molecular imaging. Roughened surface noble metal nanoparticles labeled with binding affinity molecules have also been shown to dramatically increase the Raman signal of their complementary molecules once attached through the SERS mechanism (12, 20, 21). Conjugation of monoclonal antibodies with SERS nanoparticles for targeting and imaging of specific cancer markers in live cultured cells was also recently investigated (5). Another study presents the first *in vivo* application of SERS for glucose measurements in a rat (22) by s.c. implantation of functionalized SERS nanospheres.

Recent publications have reviewed the rapid increase of Raman spectroscopy in many biomedical applications (23–25). One report has demonstrated the ability of Raman spectroscopy to diagnose benign and malignant excised breast tissue with high sensitivity and specificity (26). Another article discusses the potential of Raman spectroscopy to analyze the morphologic composition of atherosclerotic coronary artery lesions and assess plaque instability and disease progression *in vivo* (27). The recent development of a highly efficient Raman optical fiber probe has now bridged the gap between Raman spectroscopy and the clinical setting. The optical fiber probe has successfully demonstrated its usefulness in assessing human tissue models for disease and thus has great potential as a clinically practical technique (28, 29). In particular, this Raman optical fiber probe has the potential of being an extremely useful tool in an intraoperative setting, for instance in surgical debulking of cancers. Its ultra-high sensitivity would be useful in detecting even the smallest presence of malignant tissues in the human body for excision. By using targeted SERS nanoparticles and noninvasive *in* vivo imaging, Raman spectroscopy can become an important clinical diagnostic tool, as demonstrated in this article.

Biodistribution of these Raman nanoparticles are currently being evaluated in our lab with the use of radiolabels (e.g., with positron emitters) so that quantification of exact nanoparticle concentration can be explored as we have recently done with radiolabeled quantum dots (30). Additional work with tissue targeting of the Raman nanoparticles (SERS and SWNTS) should also help to further expand the eventual utility of the strategies developed in this work. Further studies with both SERS and SWNTS will still be needed to understand any potential limitations, including delivery due to nanoparticle size, optimal injected dose, and potential for toxicity. Just as quantum dots are finding increasing applications for imaging of small-animal models (31–33), so should Raman nanoparticles lead to increasing applications without the limitations faced by conventional fluorescence imaging. Furthermore, the high sensitivity associated with our modified Raman microscope in conjunction with SERS nanoparticles (8.125 pM) represents an important advantage over the sensitivity of conventional fluoroscopy imaging devices in conjunction with quantum dots [$\approx$11 nM, using IVIS (Xenogen) and Maestro (CRi, Inc.) imaging systems (unpublished data)]. Additional comparisons between quantum dots and Raman nanoparticles should help to further demonstrate the true advantages of each technique. Although no single molecular imaging strategy (including Raman) is optimal for all biological models, the use of the current Raman imaging strategy along with existing optical and nonoptical strategies should help expand the available toolbox for the field of molecular imaging. In addition, we are developing new Raman spectroscopy instrumentation for dedicated imaging of small living subjects, which should lead to faster image acquisition times; the potential to estimate signal depth; and, eventually, tomographic imaging. Further optimized instrumentation and more studies with various Raman nanoparticles should help to markedly expand the use of Raman imaging of small living subjects and should also impact newer clinical imaging strategies. The current work sets the foundation for future studies and supports continued investigation of Raman imaging of living subjects.

Methods

Raman Imaging Setup. The Renishaw InVia Raman microscope, shown in Fig. S1, consisted of a semiconductor diode near-infrared laser that operates at 785 nm and delivers 60 mW to the sample. Light was guided through a collimator onto a series of mirrors that focused the light through an open field 12$\times$ microscope lens. The mouse was illuminated with the laser beam. Light from the illuminated spot was collected with a lens and sent through a monochromator. Rayleigh scattering close to the laser line was filtered through an edge filter. The remaining inelastic (Raman) scattered light was then focused through a slit (100-μm width) and dispersed by a diffraction grating (600 grooves per millimeter) onto a CCD detector (deep depletion, PE-cooled to -70°C, with a size of 576 by 384 pixels; each pixel size is 22 $\times$ 22 μm), which then sends the detected Raman spectra to a workstation for further processing.

SERS and SWNT Nanoparticles. SERS active nanoparticles (Nanoplex Biotags; Oxonica) consisted of gold nanoparticles covered with a layer of Raman-active material and coated with glass. For more details on the structures of these SERS nanoparticles, please see Fig. S11 and *SI Text*. The SWNTS were provided by H. Dai (Stanford University, Stanford, CA) and had dimensions of a few nanometers in diameter and $\approx$200 nm in length (Fig. S1*c*).

Animal Experiments. Female 8-week-old nude mice (Charles River Laboratories) were used for all Raman spectroscope studies. All procedures performed on the animals were approved by the Stanford University Institutional Animal Care and

Use Committee and were within the guidelines of humane care of laboratory animals.

Animal Injections. Four mice were s.c. injected with 13 fmol of SERS nanoparticles in a 20-μl volume, using a 26 gauge needle. Four separate mice were injected via tail-vein with 260 fmol of SERS nanoparticles in a 200-μl volume, using a 26-gauge needle. Four additional mice were injected via tail-vein with 60 pmol of SWNTs in a 200-μl volume, using a 26 gauge needle.

Mouse Tumor Model. U87MG human glioblastoma (American Type Culture Collection) were cultured under standard conditions. The U87MG tumor models were generated by a s.c. injection of 20×10^6 cells in 200 μl of PBS near the right shoulder of the mice. Six female nude mice were inoculated with a s.c. injection near the right shoulder. When the tumor volume reached $\approx$200 mm^3, three mice were tail-vein injected with RGD SWNTs (experimental group), and three mice were injected with plain SWNTs (control group). *In vivo* Raman spectroscopic measurements were taken of the tumor site in living mice 24 h after IV injection to evaluate accumulation of RGD versus plain SWNTs in the tumor.

Preparation and Conjugation of Pegylated SWNTs with RGD. Single-wall nanotubes were prepared as described by Liu *et al.* A detailed description of RGD chemistry conjugation is provided in ref. 10. The SWNT were provided by H. Dai and have dimensions of a few nanometers in diameter and $\approx$200 nm in length yielding a concentration of 300 nM and a molecular mass of 170 kDa.

Raman Spectroscopic Imaging in Living Mice. Raman measurements were performed with a Renishaw microscope system. A semiconductor diode near-infrared laser operating at $\lambda = 785$ nm was used as the excitation source with a laser power of 60 mW measured at the surface of the mouse's skin (exposure limits in *SI Text*). Raman images were obtained by using a Raman point-mapping method. A computer-controlled *x–y* translation stage was used to raster-scan the mouse, creating a spectral image by measuring the Raman spectrum of each individual pixel in the area of interest with 500-μm, 750-μm, or 1-mm step sizes. Integration times of 3 s per step were used to acquire our Raman maps (see *SI Text* for more details). The objective lens used was a 12$\times$ open field in a dimly lit room.

Quantitative Spectral Analysis. The direct classical least squares method, also called linear un-mixing and *K*-matrix methods, was used in this work to perform a quantitative analysis of Raman spectroscopy (34, 35). More details are provided in *SI Text*.

ACKNOWLEDGMENTS. We thank Drs. Bill Doering, Glenn Davis, Ian Walton and David Guagliardo at Oxonica for their assistance with Nanoplex biotags; Dr. Zhenhuan Chi (Rensihaw) and Dr. Timothy Doyle (Stanford Small Animal Imaging) for their support. This work was funded in part by National Cancer Institute Center of Cancer Nanotechnology Excellence Grant U54 CA119367, National Institute of Biomedical Imaging and BioEngineering Bioengineering Research Partnership Grant 5-RO1-EBB000312, and ICMIC P50 CA114747 (to S.S.G.) and National Institutes of Health Training Grant T32 CA09695-15 Advanced Techniques for Cancer Imaging (to C.Z.).

1. Blasberg RG (2003) Molecular imaging and cancer. *Mol Cancer Ther* 2:335–343.
2. Gambhir SS (2002) Molecular imaging of cancer with positron emission tomography. *Nat Rev Cancer* 2:683–693.
3. Massoud TF, Gambhir SS (2003) Molecular imaging in living subjects: Seeing fundamental biological processes in a new light. *Genes Dev* 17:545–580.
4. Weissleder R (2006) Molecular imaging in cancer. *Science* 312:1168–1171.
5. Lee S, *et al.* (2007) Biological imaging of HEK293 cells expressing PLCgamma1 using surface-enhanced Raman microscopy. *Anal Chem* 79:916–922.
6. Faulds K, Barbagallo RP, Keer JT, Smith WE, Graham D (2004) SERRS as a more sensitive technique for the detection of labelled oligonucleotides compared to fluorescence. *Analyst* 129:567–568.
7. Nie S, Emory SR (1997) Probing single molecules and single nanoparticles by surface-enhanced raman scattering. *Science* 275:1102–1106.
8. Fleischmann M, Hendra PJ, McQuillan AJ (1974) Raman spectra of pyridine adsorbed at a silver electrode. *Chem Phys Lett* 26:163–166.
9. Jorio A, Saito R, Dresselhaus G, Dresselhaus MS (2004) Determination of nanotubes properties by Raman spectroscopy. *Philos Trans Roy Soc London Ser A* 362:2311–2336.
10. Liu Z, *et al.* (2007) *In vivo* biodistribution and highly efficient tumour targeting of carbon nanotubes in mice. *Nature Nanotech* 2:47–52.
11. Lacerda L, Bianco A, Prato M, Kostarelos K (2006) Carbon nanotubes as nanomedicines: From toxicology to pharmacology. *Adv Drug Deliv Rev* 58:1460–1470.
12. Mulvaney SP, Musick MD, Keating CD, Natan MJ (2003) Glass-coated, analyte-tagged nanoparticles: A new tagging system based on detection with surface-enhanced Raman scattering. *Langmuir* 19:4784–4790.
13. Yang R, *et al.* (2006) Single-walled carbon nanotubes-mediated *in vivo* and *in vitro* delivery of siRNA into antigen-presenting cells. *Gene Ther* 13:1714–1723.
14. McDevitt MR, *et al.* (2007) Tumor targeting with antibody-functionalized, radiolabeled carbon nanotubes. *J Nucl Med* 48:1180–1189.
15. Popielarski SR, Hu-Lieskovan S, French SW, Triche TJ, Davis ME (2005) A nanoparticle-based model delivery system to guide the rational design of gene delivery to the liver. 2. *In vitro* and *in vivo* uptake results. *Bioconjugate chemistry* 16:1071–1080.
16. Meyer A, Auernheimer J, Modlinger A, Kessler H (2006) Targeting RGD recognizing integrins: Drug development, biomaterial research, tumor imaging and targeting. *Curr Pharm Des* 12:2723–2747.
17. Troy T, Jekic-McMullen D, Sambucetti L, Rice B (2004) Quantitative comparison of the sensitivity of detection of fluorescent and bioluminescent reporters in animal models. *Molecular imaging* 3:9–23.
18. Souza GR, *et al.* (2006) *In vivo* detection of gold-imidazole self-assembly complexes: NIR-SERS signal reporters. *Anal Chem* 78:6232–6237.
19. Sitjtsema NM, Duindam JJ, Puppels GJ, Otto C, Greve JM (1996) Imaging with extrinsic Raman labels. *Appl Spec* 50:545–551.
20. Moskovits M (2005) Surface-enhanced Raman spectroscopy: A brief retrospective. *J Raman Spectrosc* 36:485–496.
21. Driskell JD, *et al.* (2005) Low-level detection of viral pathogens by a surface-enhanced Raman scattering based immunoassay. *Anal Chem* 77:6147–6154.
22. Stuart DA, *et al.* (2006) *In vivo* glucose measurement by surface-enhanced Raman spectroscopy. *Anal Chem* 78:7211–7215.
23. Choo-Smith LP, *et al.* (2002) Medical applications of Raman spectroscopy: From proof of principle to clinical implementation. *Biopolymers* 67:1–9.
24. Eikje NS, Aizawa K, Ozaki Y (2005) Vibrational spectroscopy for molecular characterisation and diagnosis of benign, premalignant and malignant skin tumours. *Biotechnol Annu Rev* 11:191–225.
25. Hanlon EB, *et al.* (2000) Prospects for *in vivo* Raman spectroscopy. *Phys Med Biol* 45:R1–R59.
26. Haka AS, *et al.* (2005) Diagnosing breast cancer by using Raman spectroscopy. *Proc Natl Acad Sci USA* 102:12371–12376.
27. Buschman HP, *et al.* (2001) Diagnosis of human coronary atherosclerosis by morphology-based Raman spectroscopy. *Cardiovasc Pathol* 10:59–68.
28. Motz JT, *et al.* (2004) Optical fiber probe for biomedical Raman spectroscopy. *Appl Opt* 43:542–554.
29. Motz JT, *et al.* (2005) Real-time Raman system for *in vivo* disease diagnosis. *J Biomed Opt* 10:031113.
30. Schipper ML, *et al.* (2007) microPET-based biodistribution of quantum dots in living mice. *J Nucl Med* 48:1511–1518.
31. Gao X, Chung LW, Nie S (2007) Quantum dots for *in vivo* molecular and cellular imaging. *Methods Mol Biol* 374:135–146.
32. So MK, Xu C, Loening AM, Gambhir SS, Rao J (2006) Self-illuminating quantum dot conjugates for *in vivo* imaging. *Nat Biotechnol* 24:339–343.
33. Tada H, Higuchi H, Wanatabe TM, Ohuchi N (2007) *In vivo* real-time tracking of single quantum dots conjugated with monoclonal anti-HER2 antibody in tumors of mice. *Cancer Res* 67:1138–1144.
34. Haaland DM, Easterling RG (1980) Improved sensitivity of infrared spectroscopy by the application of least squares methods. *Appl Spec* 34:539–548.
35. Pelletier MJ (2003) Quantitative analysis using Raman spectroscopy. *Appl Spect* 57:20A–42A.